

Mapping Spatiotemporal Molecular Distributions Using a Microfluidic Array

N. Scott Lynn,[†] Stuart Tobet,[‡] Charles S. Henry,[§] and David S. Dandy^{†,*}

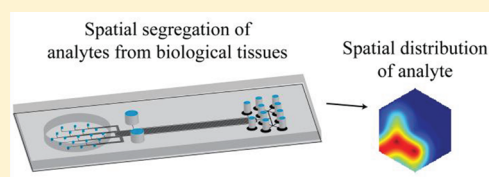
[†]Department of Chemical and Biological Engineering, Colorado State University, 1370 Campus Delivery, Fort Collins, Colorado 80523, United States

[§]Department of Chemistry, Colorado State University, 1872 Campus Delivery, Fort Collins, Colorado 80523, United States

[‡]Department of Biomedical Sciences, Colorado State University, 1680 Campus Delivery, Fort Collins, Colorado 80523, United States

S Supporting Information

ABSTRACT: The spatial and temporal distributions of an extensive number of diffusible molecules drive a variety of complex functions. These molecular distributions often possess length scales on the order of a millimeter or less; therefore, microfluidic devices have become a powerful tool to study the effects of these molecular distributions in both chemical and biological systems. Although there exist a number of studies utilizing microdevices for the creation of molecular gradients, there are few, if any, studies focusing on the measurement of spatial and temporal distributions of molecular species created within the study system itself. Here we present a microfluidic device capable of sampling multiple chemical messengers in a spatiotemporally resolved manner. This device operates through spatial segregation of nanoliter-sized volumes of liquid from a primary sample reservoir into a series of analysis microchannels, where fluid pumping is accomplished via a system of passive microfluidic pumps. Subsequent chemical analysis within each microchannel, achieved via optical or bioanalytical methods, yields quantitative data on the spatial and temporal information for any analytes of interest existing within the sample reservoir. These techniques provide a simple, cost-effective route to measure the spatiotemporal distributions of molecular analytes, where the system can be tailored to study both chemical and biological systems.



The spatial and temporal distributions of diffusible molecules play an important role in a wide variety of biological and chemical processes. The formation and maintenance of these distributions is a complex function of the local fluid convection profiles, the diffusivities of the chemicals in question, and chemical reactions that take place. There are many applications in which these chemical distributions possess characteristic length scales on the order of 1–1000 μm . Consequently, there have been a large number of studies focused on the use of microfluidic devices for the creation and multipurpose utilization of chemical gradients.^{1–3} The overall characteristics of these spatiotemporal chemical distributions often dictate the eventual outcome of many chemical and biological processes.

For nonbiological purposes, the presence of stable chemical distributions is a critical feature that drives the performance of many microfluidic reactor devices. Applications in which proper chemical gradients are required include the photopolymerization of hydrogel materials,^{4,5} the controlled crystallization of material onto a patterned substrate,⁶ the stereoselective control of chemical reactions,⁷ and the combinatorial synthesis of CdSe nanoparticles.⁸ In all of these cases, spatial characteristics of one or more chemical distributions is the primary factor dictating the success or failure of the device; therefore the ability to quantify the spatial distributions of key chemicals within a microreactor is of high value.

The importance of chemical distributions within biological systems are, by far, much larger in scope, both in the overall

number of applications as well as the complexity of each system.⁹ The spatiotemporal distributions of an extensive number of signaling molecules in biological systems drive a variety of complex functions, ranging from the stimulated release of oocytes from ovaries¹⁰ and the migration of neurons in the developing brain,^{11,12} to the development of vasculature.¹³ The evolution of these spatiotemporal molecular gradients is regulated via a number of physical and biological mechanisms, which may include passive diffusion, cell secretion and uptake, enzymatic reaction or chemical degradation, inhibitor/competitor interactions, and the interaction between specific molecules with the surrounding intercellular matrix. While there exists a large amount of research studying the effects of a chemical stimuli distribution of the outcome of a biological system,^{14–16} the precise effects of many signaling molecules on cell differentiation, growth, and chemotaxis remain largely unknown.¹⁷ Development of new analysis techniques to quantify key chemical components with high spatial and temporal resolution will provide a better understanding of how external stimuli influence the spread of chemical signals.

Despite the abundance of research pertaining to the use of (bio)microfluidic devices for the study of chemical distributions

Received: August 31, 2011

Accepted: November 29, 2011

toward chemical and biological applications, nearly all focus on the controlled creation of a primary gradient while ignoring secondary gradients that might result from chemical or biological interactions.¹⁸ Perhaps the biggest challenge in this area is the inability to sample multiple chemical messengers across the spatial extent of a fluidic region. Spatiotemporal measurements of applicable gradients have almost exclusively relied on fluorescence microscopy toward the measurement of a single chemical species, a technique that is limited to at most only a few chemical species. The ability to measure multiple chemical messengers with ample spatial resolution from a fluidic region requires the ability to sample small volumes of fluid near (or in) the tissue slice with high accuracy. This sampling capability requires a high degree of precision in several areas, including (i) collecting fluid from multiple locations at known positions, (ii) controlling flow rates such that the areas of tissue from which fluid is collected between measurement positions have minimal overlap, and (iii) quantifying the presence of multiple chemical analytes from each measurement position. Performing this type of analysis with existing commercial instrumentation is theoretically possible; however, the size and expense of the equipment would lie outside the range available to most laboratories. Due to their small length scales, analysis times, and high spatial precision, microfluidic devices provide a convenient and cost-effective solution that addresses all three precision requirements.

Here we present a microfluidic device capable of sampling multiple chemical messengers with a spatial resolution dictated by the extent and overall architecture of a simple microfluidic network (μ FN). This spatial sampling reservoir is shown in Figure 1, where sample ports on the floor of a larger reservoir

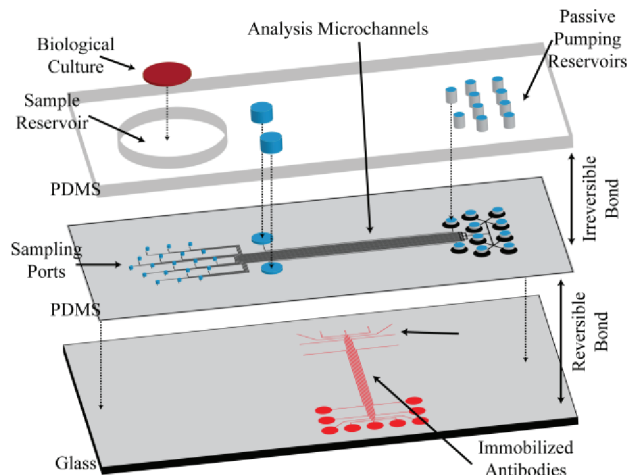


Figure 1. Overall diagram of the spatial microfluidic sampler. The top two PDMS layers are irreversibly bonded to one another, with thicknesses of 4.5 mm and 0.4 mm for the upper and lower layers, respectively, providing an overall height of the passive pumping reservoirs of $H = 4.9$ mm. A $110 \mu\text{m}$ punch is used to create the vertical sample ports connecting the sample reservoir to the underlying μ FN.

lead to a μ FN on the bottom face of a simple polydimethylsiloxane (PDMS) construct. Due to the precise fabrication methods of the underlying microfluidic architecture, the position of each sampling port can easily be modified to sample fluid from specific regions of interest within the sample

reservoir. The device is readily fabricated using soft lithographic processes, where the degree of fluid sampling from each port is controlled via passive pumping techniques. The system is compatible with most transduction mechanisms that are easily incorporated into planar microfluidic systems, leading to a cost-effective solution for high-resolution, multianalyte chemical analysis. For a proof of concept experiment we utilize fluorescent imaging to demonstrate the ability of the device to sample fluid spatially across the floor of the small sample reservoir. We then apply this microfluidic device in a heterogeneous immunoassay format directed toward the simultaneous spatial resolution of two proteins situated in different locations within the reservoir.

MATERIALS AND METHODS

Diagrams of the spatial sampling μ FN, details for the measurement of volumetric flow rates vs time, details for the real-time spatial assay, and details for the multiple analyte spatially resolved micromosaic assay are in the SI. Human blood plasma was obtained by drawing 15 mL of venous blood into a Vacuette K3E tube (Greiner Bio-One). After gentle mixing the whole blood was centrifuged at 3600 rpm for 10 min (4°C), after which the plasma drawn from the top of the tube and stored at -80°C until use. The growth media consisted of neurobasal medium (Invitrogen) with B27 supplement (GIBCO BRL Laboratories), and supplemented with 0.025 mM glutamate, and 0.5% w/w glucose.¹⁹ The real-time and immunoassay protocols utilized 45 mg mL^{-1} solutions of BSA (Sigma) in phosphate buffered saline (Sigma), with fresh solutions prepared weekly. Fluorescent images were obtained with an inverted microscope with an epifluorescence attachment (Nikon TE-2000) and fitted with a CCD camera (CoolSnap fx) using custom Matlab software.

The μ FNs used here were fabricated using soft lithography and rapid prototyping.²⁰ After curing of the PDMS molds, a high-precision biopsy punch (Technical Innovations) was used to create $110 \mu\text{m}$ diameter sampling ports through a 0.4 mm thick PDMS layer leading to the μ FN on the lower side. This lower PDMS layer was then aligned and plasma bonded (900 mTorr, 20 W, 18 s) to an upper PDMS layer with a 1 cm diameter reservoir created with a standard punch (Robbins). After bonding, the two layers were placed in a 65°C oven for 2 h. Passive pumping reservoirs were then created with a 1.05 mm diameter high-precision biopsy punch, where anywhere from 1 to 8 pumping reservoirs were punched. The plug formed from punching the sample reservoir was then reinserted (to keep the sample reservoir walls hydrophobic), and the μ FN was exposed to oxygen plasma and sealed to a bottom substrate. After oxidation, the spatial sampler was then placed into a 200 mtorr vacuum for 25 min, which acts to facilitate the process of filling via capillary action.²¹ After removal from the vacuum chamber, $250 \mu\text{L}$ of aqueous media was delivered to the sample reservoir, followed by $100 \mu\text{L}$ of mineral oil to eliminate evaporation, after which filling of the μ FN via capillary action typically was completed within 1 min. No priming of the pumping reservoirs was required.

RESULTS

Design and Operation of the Spatial Sampling Reservoir. The design of our spatial sampling reservoir is detailed in Figure 1. The reservoir is composed of a two layer PDMS system, where (i) a large (1 cm) diameter hole in the

top layer comprises the vertical sidewalls of a sample reservoir, and (ii) 110 μm diameter vertical sampling ports lead to a μFN on the bottom side of the lower layer, created using soft lithographic techniques. After the two PDMS layers have been irreversibly bonded to one another, the entire structure can be sealed (irreversibly or reversibly) to a variety of substrates. After sealing of the PDMS structure to a lower substrate and introduction of liquid into the sample reservoir, capillary action rapidly fills the entire microfluidic network provided the sampling ports and microchannels are sufficiently hydrophilic. After filling, liquid continues to flow through the μFN via a network of passive microfluidic pumps,²² where a single channel connecting the pumps to the analysis microchannels serves to create comparable pressure gradients across the length of each channel. The volumetric flow rate through each microchannel is a function of the overall geometry of individual channels, where precise control over flow rates is accomplished by varying the width, height, or length of each channel.

The spatial sampler shown in Figure 1 is designed to quantify the spatial distribution of chemicals situated near the array of sampling ports. The operating mechanisms of this device regarding chemical and biological applications are equivalent. For simplicity we will restrict our discussion to biological based applications. Here, signal molecules secreted from cells or organotypic tissue pieces lying on the floor of the sample reservoir will be drawn into a sampling port positioned near the point of secretion. The resulting concentration of a signaling molecule within each analysis microchannel will therefore be a function of several parameters, including the volumetric flow rate through each microchannel, the spatial secretion flux of the molecule, and the geometry and positioning of the sample ports. Through the precision of soft lithographic rapid prototyping,²⁰ we can maintain a high degree of control over geometric parameters and volumetric flow rates.²² Therefore, knowing the positions of each sampling port, the spatial distribution of signaling molecule secretion rates may be inferred from the concentration of those molecules in their respective analysis microchannels. The results shown in this study pertain to distributions of chemicals within a sample reservoir; however, it should be noted that these methods are also effective for measuring the distributions of chemicals in a flow cell constructed in place of the sample reservoir.

Long-term, Steady-state Passive Pumping. In this study, the regulation of the fluid flow rate (Q) through the analysis microchannels is determined by the geometries associated with multiple passive pumping reservoirs operating in parallel. These pumps consist of small vertical reservoirs (ranging from 0.1 to 2 mm in diameter) at the terminal end of the microfluidic network connected to the sample reservoir. The fundamental mechanisms involving the operation of these pumps have been described previously.²² Briefly, after introduction of liquid in to an inlet reservoir, capillary action fills the microfluidic network to the point that a small meniscus is formed around the bottom corners of each pumping reservoir. The Laplace pressure created by this curved interface will then fill each reservoir to the point at which the volumetric fluid flow rate through the microchannels is balanced by the rate of evaporation of water from the air/liquid meniscus, at which point the flow becomes steady. The steady-state volume of liquid in each pumping reservoir (V_{ss}) and volumetric flow rate (Q_{ss}) are therefore dependent on a number of parameters, including the overall viscous resistance of the microfluidic network connecting the pumps to the sample reservoir, the

overall diameter and height of each pumping reservoir, the viscosity and volatility of the fluid, and the temperature and relative humidity of the surrounding environment.

For purposes of robustness, it is important to be able to pump the multitude of solutions associated with biological systems, where the range of fluids encountered vary from being simple and dilute (phosphate buffered saline) to complex in nature (growth media, blood serum). This complexity can be problematic for this passive pumping technique due to both the presence of the air/water interface and the large surface area to volume ratio inherent at the microscale.²³ In particular, small amounts of evaporation can often lead to solute crystallization and the overall failure of the pumping process.

One simple method to prevent solute crystallization is to maximize the space time τ of the reservoir, where τ is defined as $\tau = V_{ss}/Q_{ss}$. Essentially, solutes within pumping reservoirs with a large value of τ will become concentrated less rapidly than those in a reservoir with a smaller value of τ . For pumping reservoirs with common diameters connected to μFN s of equal viscous resistance K (defined in the SI), one can simultaneously increase V_{ss} and lower Q_{ss} by increasing the height of the reservoir H , defined as the overall height of the pumping reservoirs (Figure 1). This effect is demonstrated in Figure 2,

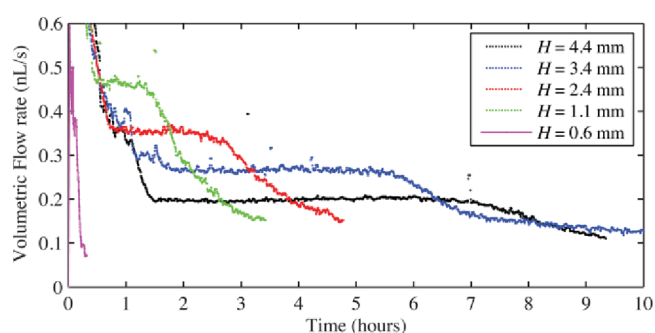


Figure 2. Flow rate versus time for passive pumping of human blood plasma for different values of the reservoir height H . The microchannel had a width, height, and length of 100 μm , 26 μm , and 15 mm, respectively ($K = 1.8 \times 10^5 \text{ g mm}^{-4} \text{ s}^{-1}$), with a single 1.0 mm diameter passive pumping reservoir.

where pseudoinstantaneous particle tracking methods were used to measure Q versus time (t) for passive pumping of human blood plasma solutions through microchannels of equal dimensions while varying H . Each of the plots shown in Figure 2 exhibit an initial unsteady period during which the pumping reservoir is filling with liquid. In this period Q will decrease until the liquid volume (V) of fluid in each reservoir reaches a point where $V = V_{ss}$, after which fluid will be pumped in a steady-state manner until any solutes reach saturated concentrations and bulk crystallization occurs. After this point the flow again becomes unsteady and will slowly decay to zero. As expected, it can be seen from Figure 2 that as the pumping reservoir height increases, there is a decrease in Q_{ss} in addition to an increase in both the time for the system to reach steady-state as well as the duration in which the system remains steady. The stability of this flow is noteworthy; for example, the $H = 4.4 \text{ mm}$ reservoir maintains a steady flow of $Q = 0.200 \pm 0.013 \text{ nL s}^{-1}$ between 1.5 and 6.5 h, a significant achievement considering the complex nature of human blood plasma (7% solids).

Although the results in Figure 2 display a high degree of control over the steady-state volumetric flow rate by varying the height of the PDMS pumping reservoirs, it is desirable to possess control over Q_{ss} without sacrificing the duration of steady flow. Here we show the ability to control the volumetric flow rate through a μ FN via the use of multiple passive pumping reservoirs operating in parallel. Figure 3 displays Q vs t

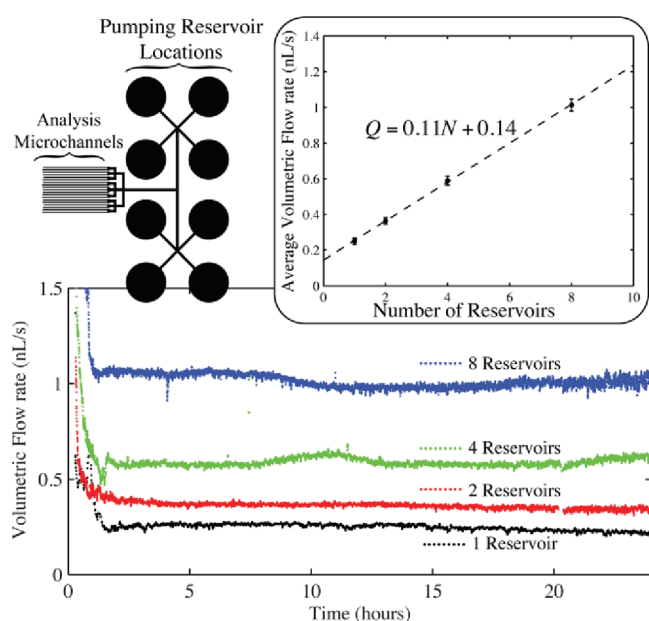


Figure 3. Q vs t regarding the passive pumping of neurobasal growth media through the spatial microfluidic sampler shown in Figure 1. The overall μ FN had a viscous resistance of $K = 2 \times 10^5 \text{ g mm}^{-4} \text{ s}^{-1}$ and an overall height of $H = 4.9 \text{ mm}$. Averages and standard deviations of these data sets were used to create the inset ($1 < t < 24 \text{ h}$), highlighting the linear relationship between Q_{ss} and the number of pumping reservoirs N .

pertaining to passive pumping of biological growth media through the spatial microfluidic sampler shown in Figure 1 ($H = 4.9 \text{ mm}$). The outlet regions of the spatial assay μ FN contains 8 locations in which a reservoir can be located, where the

reservoirs are created using a punching process, resulting in the ability to operate the assay using anywhere from 1 to 8 reservoirs. It can be seen from Figure 3 that increases in Q_{ss} are achieved by increasing the number of pumping reservoirs in operation, where steady-state flow is maintained for 24 h in all cases. The inset in Figure 3 displays the average volumetric flow rate for each data set ($1 < t < 24 \text{ h}$) as a function of the number of reservoirs (N) in operation; the relationship between Q and N is clearly linear. It is expected that provided a satisfactory μ FN design, this relationship can be extrapolated indefinitely to higher values of N . Spatial assays of this design reach a steady-state within 1 h and have been observed to operate at steady state for over 45 h. The source of the slight deviations in $Q(t)$ shown in Figure 3 are not known and might be due to several factors, including imperfections in the passive pumping reservoir sidewalls and/or uncontrolled changes in temperature/humidity in the external environment. These deviations, however, do not exceed 10% of the mean and are not expected to have a large effect on the outcomes of the spatial assays discussed in the following sections.

Real-time Spatial Assay. The ability of the spatial microfluidic assay to obtain pseudo real-time data concerning the spatial distribution of an analyte was demonstrated with a simple proof-of-concept experiment. After filling the sample reservoir with a 45 mg mL^{-1} bovine serum albumin (BSA) solution and allowing the passive pumping process enough time to reach steady-state, a GC syringe attached to a micro-manipulator was used to inject a $0.3 \mu\text{L}$ plug of 0.2 mg mL^{-1} fluorescently tagged IgG in a precise location just above the floor of the sample reservoir. A fluorescent microscope was then used to monitor the average fluorescent intensity across 19 analysis microchannels, each collecting fluid from a precise location from the floor of the sample reservoir (2 mm pitch, close packed). In this case the steady state flow rate through the entire μ FN was measured to be 1.2 nL s^{-1} , with the imaging region situated 2 mm from the point of conjunction of the analysis microchannels. The average fluorescent intensity of all 19 channels were calculated from images taken once every 30 s, and knowledge of the μ FN geometry was used to correct each time series signal for the average time delay for fluid to travel from the floor of the reservoir to the imaging region within

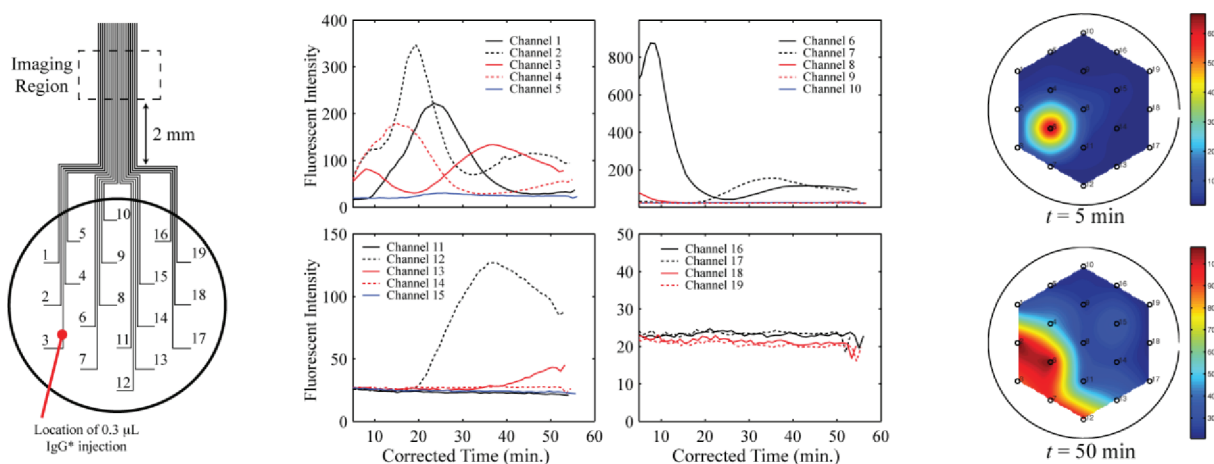


Figure 4. (Left) Ordering of the analysis microchannels for the μ FN used in this study. After establishing a steady-state flow rate of 1.2 nL s^{-1} of a BSA solution (45 mg mL^{-1} in PBS), a $0.3 \mu\text{L}$ plug of fluorescent IgG was injected into the reservoir. The real-time analysis of fluorescent intensity in all 19 analysis channels was then monitored over time (middle). These time-corrected fluorescent data are then analyzed with a simple interpolation scheme to estimate the fluorescent species distribution near the reservoir floor (right).

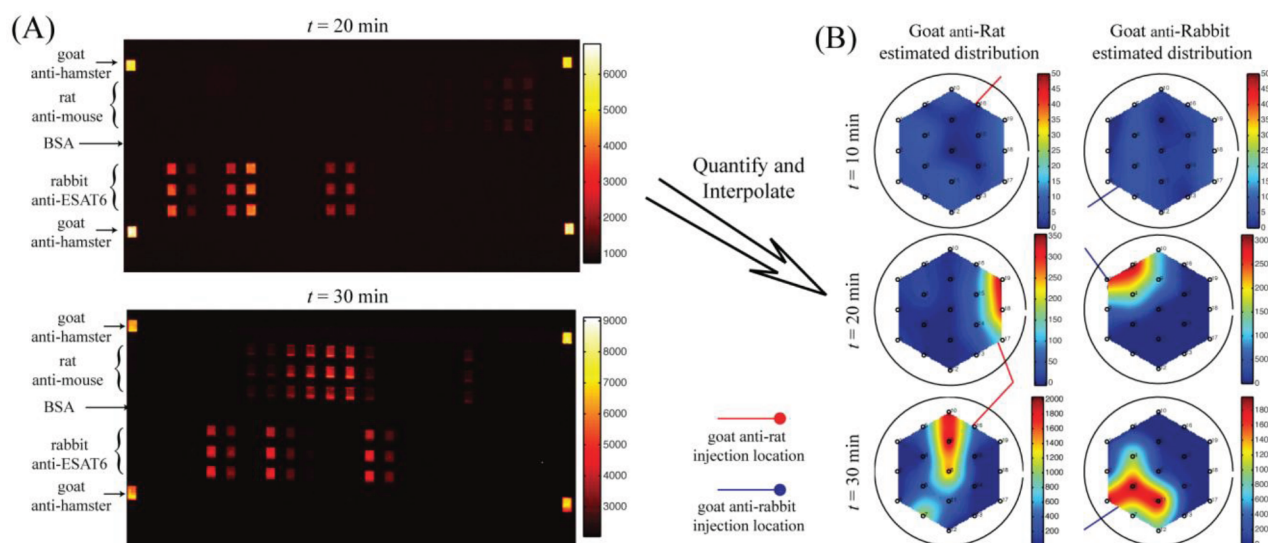


Figure 5. (A) Discrete experiment similar to that shown in Figure 4. The spatial microfluidic assay was reversibly bonded to a substrate with antigens immobilized in discrete stripes orthogonal to the analysis microchannels. Two separate $0.3 \mu\text{L}$ injections of anti-rat and anti-rabbit (0.67 mg mL^{-1}) were injected in different locations into the sample reservoir. Steady state flow through the μFN was $Q_{\text{ss}} = 0.59 \text{ nL s}^{-1}$. The fluorescent images on the left show good spatial resolution between the two analyte species. (B) Fluorescent image is then quantified, corrected for background, and used in a simple interpolation scheme to estimate the species spatial distribution in the sample reservoir. Three assays of $t = 10, 20,$ and 30 min are shown.

each microchannel (detailed in the SI). This time correction is required due to the specific design of this μFN , where an optimized μFN would not require time corrected data.

Figure 4 plots the average fluorescent intensity vs the corrected time (t_{corr}) for all of the 19 analysis microchannels individually corrected for delay. The $0.3 \mu\text{L}$ fluorescent IgG injection was delivered to a location within the region enclosed by sample ports 2, 3, and 6. From the plots in Figure 4, it can be seen that the fluorescent signal is initially isolated to channels 2, 3, and 4 with a much higher intensity in channel 6 ($t < 10$ min). After time the fluorescent protein occupies several other channels with varying intensity, where the intensity for each channel is dependent on both time and the distance from the initial injection. To visualize the 19 time-series signals shown in Figure 4, a two-dimensional (2D) interpolation scheme was used with the time corrected data to estimate the spatial distribution of the IgG across the floor of the reservoir (details in the SI). Figure 4 (right) plots the 2D spatial resolution of the fluorescent IgG at times of 5 and 50 min after injection using the time-corrected data. Due to the geometric layout of the sampling ports and interpolation scheme, the estimated spatial distribution of dye is limited to the hexagonal region bound by the external sample ports; however, this problem can be addressed through the use of multiple sample ports along the bottom edge of the reservoir. For purely diffusive transport ($D_{\text{IgG}} = 4.3 \times 10^{-11} \text{ m}^2 \text{ s}^{-1}$), the IgG is expected to travel a mean squared distance of approximately 0.8 mm one hour after the injection. From the contour plots shown in Figure 4, the IgG travels approximately 4 mm from the injection location in the span of less than one hour, indicating there is a small degree of convection present in the reservoir, most likely due to the small degree of fluid withdrawal through the 19 sampling ports. The results shown in Figure 4 highlight the spatial resolution capabilities of this microfluidic system, where spatial measurements are made with a resolution of 2 mm. It is expected that the spatial resolution of these measurements can be readily increased with the use of analysis microchannels on a smaller pitch.

Multiple Analyte Spatially Resolved Micromosaic Assay.

Here we show the capability of this system to provide spatial resolution of multiple analytes using experiments in discrete time through the use of micromosaic immunoassays.²⁴ The design of a two-analyte micromosaic immunoassay using the spatial sampling chamber is accomplished as follows. First, a separate μFN was used to covalently immobilize three sets of antigens to a functionalized glass slide in discrete, $40 \mu\text{m}$ wide stripes, in a pattern as seen in Figure 1.²⁵ In this case, two of the antigens are used for spatial detection purposes (rat, rabbit IgG) while a third is used for alignment purposes (goat IgG). After passivation of the glass slide with BSA, a spatial assay similar to that used in Figure 1 was rendered hydrophilic and reversibly sealed to the glass slide in a manner such that the analysis microchannels orthogonal to the immobilized antigen stripes. After filling the sample reservoir with a solution of 45 mg mL^{-1} BSA in PBS and allowing the flow to reach steady state, a GC syringe and a micromanipulator were used to inject two separate $0.3 \mu\text{L}$ plugs of 0.67 mg mL^{-1} fluorescently tagged IgG (anti-rat, anti-rabbit) in different locations just above the reservoir floor. Here, four passive pumping reservoirs were used to generate a total steady state volumetric flow rate of 0.59 nL s^{-1} ($H = 4.9$ mm). Next, a solution of anti-goat IgG was introduced separately into two alignment channels situated along both sides of the analysis microchannels. The assay was allowed to proceed for a predetermined time ($t = 10, 20, 30$ min), after which the glass slide was peeled from the PDMS spatial assay, rinsed, dried, and imaged with a fluorescent microscope. Details on this assay can be found within the SI.

Figure 5A presents fluorescent images of the spatial micromosaic assay for assays of $t = 20$ and 30 min. The goat/anti-goat system serves both as an alignment tool for image quantification and if needed, a calibration source for the remaining antigen/antibody systems. It should be noted that the rat/anti-rat and rabbit/anti-rabbit pairs have cross-reactivity levels less than 9% (shown in the SI). Therefore, due to the design of the underlying μFN we can infer the spatial distribution of an aqueous antibody in the sample reservoir

by the distribution of fluorescent intensities of spots in each detection channel. An example of this is seen in the $t = 20$ min assay, where the anti-rabbit is found to be bound to the surface at increased levels within channels 1, 2, 4, 5, 9, and 10 (upper left side of the reservoir), whereas the anti-rat is bound at lower levels within channels 15 through 19 (right side of the reservoir). After background correction of the bound fluorescent species using the BSA control, the quantified fluorescent levels for the anti-rat and anti-rabbit IgGs in each analysis channel are used with the same interpolation scheme as in Figure 4. The estimated species distributions are shown in Figure 5B. Due to the dependence on the reversible affinity interaction between bound antigen and aqueous antibody and finite fluid velocity within each channel, the fluorescent distributions seen in Figure 5 are not an exact representation of the IgG concentration in each detection channel;²⁶ however, these signals provide clear insight into the spatial distributions of the respective antibodies near the floor of the sample reservoir, and can be easily calibrated to account for nonequilibrium effects. Also, these types of discrete data are not correctable for the delays associated with channels of different lengths as discussed above, but this is easily remedied through the use of an appropriate μ FN. It can be seen that the estimated spatial distributions of IgG in each channel have a remarkable similarity to those using the single analyte real-time assay discussed in the previous section, where the system is capable of distinguishing spatial gradients on the order of the pitch of the sampling ports. The multianalyte capability of this method is only limited by the availability of antigen/receptor pairs, as the information density regarding the images shown in Figure 5 will increase as the inverse square of the width of the underlying immobilization and analysis microchannels. Because the experiments used here rely on manual injection of analyte via a GC syringe (location of injection, speed of syringe injection), reproducibility across experiments is limited to the skill of the experimental technician; however, the reproducibility in fabrication of these devices is very high and measurements of relevant biological systems are not expected to be highly variable. For example, there is no significant difference in the long term averaged passive volumetric flow rates across multiple reservoir designs utilizing the same geometries (analysis microchannels, reservoir geometries) in a laboratory setting.

DISCUSSION

The sections above highlight the ability of this system to measure the spatial distribution of fluorescently tagged antibodies from regions close to the floor of a sample reservoir. The strength of this technique lies in the ability of the spatial sampler to segregate nanoliter-sized volumes of liquid into individual microchannels for subsequent analysis. This study utilized fluorescence microscopy as the detection mechanism for analyte quantification; however, because the positioning of the sample ports is comparatively independent from the μ FN architecture, the underlying μ FN can be readily modified to be compatible with a variety of colorimetric, optical, or electrochemical transduction mechanisms.

Applying this method to nonbiological applications is straightforward and parallels the results shown above. Utilization of this device for biological purposes presents additional minimal challenges that are discussed as follows: (i) This device is intended to measure the secretion rates of signaling molecules from a cell or tissue culture, or tissue slice

lying on the floor of the sample reservoir. Because the secretion rate of signaling molecules from a tissue slice has a dimension associated with molecular flux ($\text{mol mm}^{-2} \text{ s}^{-1}$), the concentration distribution of a secreted molecule will be a function of the secretion flux as well as the geometries and fluid flow profile associated with the space between the reservoir floor and tissue. The utilization of raised PDMS structures (or a biologically compatible membrane) on the floor of the sample reservoirs will ensure that a molecule secreted from a precise tissue location ends up flowing through the nearest sample port; furthermore, such structures can act to segregate the live cells or tissues from the sampling reservoirs and allow local convection profiles to be repeatable across samples (to be validated through use of the particle tracking methods used here). Lower flow rates in the analysis microchannels will provide higher concentrations of analyte within each analysis microchannel at the expense of a longer delay time, while higher flow rates shorten the delay time at the expense of lower analyte concentrations and potentially problematic depletion of the analyte and key signal molecules from the sample reservoir. Optimal operating conditions, analysis microchannel geometries, and sample port pitch can be explored through the use of a variety of computational methods. The fabrication techniques used in this study can provide $110 \mu\text{m}$ diameter sample ports with a minimum pitch of approximately $300 \pm 25 \mu\text{m}$, well within the accuracy of modern soft lithographic approaches. Therefore one can infer with increased accuracy the spatial and temporal secretion rate and location simply by measuring the concentration of signal molecules across all of the analysis microchannels with transduction and detection methods of choice. (ii) Nutrient delivery to *in vitro* cultures is essential for proper cell function. With this in mind, the sample reservoir shown in Figure 1 can easily be replaced with a flow cell to allow for nutrient delivery using an external syringe pump. Due to the passive nature of the pumping mechanisms used here, the volumetric flow rate through the analysis microchannels will have only a weak dependence on the flow rate through an overlying flow cell, with increases in Q_{ss} proportional to the relative increase in fluid pressure in the vicinity of the tissue slice. It should be noted that an overlying flow cell could also be used for localized chemical stimulation of an organotypic tissue slice using the methods previously described by Jeon et al.¹ (iii) In this study the spatial microfluidic sampler was utilized in two proof of concept experiments, (1) fluorescent microscopy was used for the real-time spatial analysis of a single analyte, and (2) micromosaic immunoassays were used for discrete-time spatial analysis of multiple analytes. The underlying μ FN architecture remains essentially independent of the positions of the sampling locations on the floor of the reservoir, such that it is only necessary to consider the overall viscous resistance of each channel to ensure targeted liquid flow rates. Therefore the transduction mechanism for chemical analysis is limited only to what can be fabricated within geometric constraints of the μ FN, and real-time multianalyte analysis can be achieved by a variety of methods, including fluorescent or colorimetric, electrochemical, localized optical, or enzymatic means. (iv) Perhaps the most important aspect of the device utilized in this study is the translucent nature of the PDMS/glass material. The optically clear sample reservoir allows for the use of standard microscopy methods for the measurement of macroscopic tissue processes, such as the of stimulated release of an oocyte from an organotypic ovary slice,²⁷ while simultaneously

measuring the microscopic spatial-temporal distributions of chemical messengers across the breadth of the entire tissue.

The techniques described here offer a simple, cost-effective route to measure the spatial-temporal distribution of chemical analytes situated near an array of sampling ports. In contrast to methods that measure the overall secretion (or uptake) of chemicals from single *in vitro* tissue samples,^{28,29} this approach allows for the measurement of multiple chemical messengers from multiple locations in pseudo real-time. This technique has great potential to elucidate many of the complex mechanisms involved in intercellular signaling processes, including the relationships of how external and chemical stimuli influence the spread of chemical signals.

■ ASSOCIATED CONTENT

📄 Supporting Information

Additional information as noted in text. This material is available free of charge via the Internet at <http://pubs.acs.org>.

■ AUTHOR INFORMATION

Corresponding Author

*David S. Dandy, e-mail: dandy@colostate.edu. Office: 970-491-7437. Fax: 970-491-7369.

■ REFERENCES

- (1) Jeon, N. L.; Dertinger, S. K. W.; Chiu, D. T.; Choi, I. S.; Stroock, A. D.; Whitesides, G. M. *Langmuir* **2000**, *16*, 8311–8316.
- (2) Dertinger, S. K. W.; Chiu, D. T.; Jeon, N. L.; Whitesides, G. M. *Anal. Chem.* **2001**, *73*, 1240–1246.
- (3) Irimia, D.; Geba, D. A.; Toner, M. *Anal. Chem.* **2006**, *78*, 3472–3477.
- (4) Zaari, N.; Rajagopalan, P.; Kim, S. K.; Engler, A. J.; Wong, J. Y. *Adv. Mater.* **2004**, *16*, 2133–+.
- (5) Burdick, J. A.; Khademhosseini, A.; Langer, R. *Langmuir* **2004**, *20*, 5153–5156.
- (6) Aizenberg, J.; Black, A. J.; Whitesides, G. M. *Nature* **1999**, *398*, 495–498.
- (7) Skelton, V.; Greenway, G. M.; Haswell, S. J.; Styring, P.; Morgan, D. O.; Warrington, B. H.; Wong, S. Y. F. *Analyst* **2001**, *126*, 11–13.
- (8) Toyota, A.; Nakamura, H.; Ozono, H.; Yamashita, K.; Uehara, M.; Maeda, H. *J. Phys. Chem. C* **2010**, *114*, 7527–7534.
- (9) Wu, M. H.; Huang, S. B.; Lee, G. B. *Lab Chip* **2010**, *10*, 939–956.
- (10) Otsuka, F.; McTavish, K. J.; Shimasaki, S. *Mol. Reprod. Dev.* **2011**, *78*, 9–21.
- (11) Wierman, M. E.; Kiseljak-Vassiliades, K.; Tobet, S. *Front. Neuroendocrinol.* **2011**, *32*, 43–52.
- (12) Eichmann, A.; Makinen, T.; Alitalo, K. *Genes Dev.* **2005**, *19*, 1013–1021.
- (13) Ober, E. A.; Olofsson, B.; Makinen, T.; Jin, S. W.; Shoji, W.; Koh, G. Y.; Alitalo, K.; Stainier, D. Y. R. *EMBO Rep.* **2004**, *5*, 78–84.
- (14) Young, E. W. K.; Beebe, D. J. *Chem. Soc. Rev.* **2010**, *39*, 1036–1048.
- (15) Chung, S.; Sudo, R.; Vickerman, V.; Zervantonakis, I. K.; Kamm, R. D. *Ann. Biomed. Eng.* **2010**, *38*, 1164–1177.
- (16) Salieb-Beugelaar, G. B.; Simone, G.; Arora, A.; Philippi, A.; Manz, A. *Anal. Chem.* **2010**, *82*, 4848–4864.
- (17) Hancock, J. T. *Cell signalling*, 2nd ed.; Oxford University Press: New York, 2005; pp xix, 296.
- (18) Kim, S.; Kim, H. J.; Jeon, N. L. *Integr. Biol.* **2010**, *2*, 584–603.
- (19) Tobet, S. A.; Walker, H. J.; Seney, M. L. *Integr. Comp. Biol.* **2002**, *42*, 1325–1325.
- (20) Duffy, D. C.; McDonald, J. C.; Schueller, O. J. A.; Whitesides, G. M. *Anal. Chem.* **1998**, *70*, 4974–4984.
- (21) Dimov, I. K.; Basabe-Desmonts, L.; Garcia-Cordero, J. L.; Ross, B. M.; Ricco, A. J.; Lee, L. P. *Lab Chip* **2011**, *11*, 845–850.
- (22) Lynn, N. S.; Dandy, D. S. *Lab Chip* **2009**, *9*, 3422–3429.

(23) Lynn, N. S.; Henry, C. S.; Dandy, D. S. *Lab Chip* **2009**, *9*, 1780–1788.

(24) Bernard, A.; Michel, B.; Delamarche, E. *Anal. Chem.* **2001**, *73*, 8–12.

(25) Wu, P.; Hoglebe, P.; Grainger, D. W. *Biosens. Bioelectron.* **2006**, *21*, 1252–1263.

(26) Squires, T. M.; Messinger, R. J.; Manalis, S. R. *Nat. Biotechnol.* **2008**, *26*, 417–426.

(27) Frahm, K. A.; Clay, C. M.; Tobet, S. A. *Biol. Reprod. Suppl.* **2010**, *83*, 13.

(28) van Midwoud, P. M.; Groothuis, G. M. M.; Merema, M. T.; Verpoorte, E. *Biotechnol. Bioeng.* **2010**, *105*, 184–194.

(29) van Midwoud, P. M.; Merema, M. T.; Verpoorte, E.; Groothuis, G. M. M. *Lab Chip* **2010**, *10*, 2778–2786.